

Article

Design and Study of a Sediment Erosion Test Device for a Single-Flow Channel in the Guide Apparatus of a Reaction Hydraulic Turbine

Jiayang Pang ¹, Xiao Chang ², Yuanyuan Gang ³, Ziyao Zhou ³, Wenping Xiang ⁴, Lingjiu Zhou ^{1,*} , Xiaobing Liu ^{3,*} and Zhengwei Wang ⁵ 

¹ College of Water Resources and Civil Engineering, China Agricultural University, Beijing 100083, China; pangjy@163.com

² Power China Hydropower Development Group Co., Ltd., Chengdu 610095, China

³ Key Laboratory of Fluid and Power Machinery, Ministry of Education, Xihua University, Chengdu 610039, China

⁴ Gongzui Hydropower General Plant Dadu River Co, Ltd., Leshan 641900, China

⁵ Department of Energy and Power Engineering, Tsinghua University, Beijing 100084, China; wzw@mail.tsinghua.edu.cn

* Correspondence: zlj@cau.edu.cn (L.Z.); liuxb@mail.xhu.edu.cn (X.L.)

Abstract: Sediment erosion damage is one of the main causes of structural failure in reaction turbine units. To study the mechanism through which sediment erosion affects the water-guiding mechanism of a reaction turbine unit, this study obtained the average concentration and particle size of sediment during the flood season based on the statistics of the measured sediment data from the power station. Additionally, the characteristics of the solid–liquid two-phase flow of the diversion components of the reaction hydraulic turbine were numerically calculated. Based on the velocity triangle change in the guide apparatus and the flow similarity principle, a flow-around wear test device for the guide apparatus of the reaction turbine was designed. Furthermore, the similarity of the sand–water flow field between the guide apparatus of the prototype unit and the test device was compared and analyzed. The results demonstrated that the sand–water flow field of the diversion components of the prototype unit was axisymmetric and exhibited a potential flow distribution. Additionally, uniform sand–water flow occurred within the guide apparatus, with a small sand–water velocity gradient near the wall of the stay vanes (SV) and the guide vanes (GV). The maximum volume fraction of sediment particles was observed in the tailing area of the spiral casing, indicating an enrichment phenomenon of sediment particles. The velocity of the sediment particles on the surface of the guide vane in the single-channel sediment wear test device and prototype unit ranged from 6.2 to 7.8 m/s, and the velocity of the sediment particles on the surface of the stay vane ranged from 5.1 to 14.6 m/s, and the difference of the sediment particles' velocity near the wall was 1 to 3 m/s. The trailing vorticity of the guide vane reached a maximum of 120 s^{-1} . Consequently, the single-channel sediment erosion test device can unveil the sediment erosion mechanism of the guide apparatus of a reaction turbine.



Citation: Pang, J.; Chang, X.; Gang, Y.; Zhou, Z.; Xiang, W.; Zhou, L.; Liu, X.; Wang, Z. Design and Study of a Sediment Erosion Test Device for a Single-Flow Channel in the Guide Apparatus of a Reaction Hydraulic Turbine. *J. Mar. Sci. Eng.* **2024**, *12*, 777. <https://doi.org/10.3390/jmse12050777>

Received: 29 March 2024

Revised: 24 April 2024

Accepted: 29 April 2024

Published: 7 May 2024



Copyright: © 2024 by the authors. Licensee MDPI, Basel, Switzerland. This article is an open access article distributed under the terms and conditions of the Creative Commons Attribution (CC BY) license (<https://creativecommons.org/licenses/by/4.0/>).

Keywords: sediment erosion; guide apparatus; numerical calculation; solid–liquid two-phase flow; similarity principle; flow-around erosion test

1. Introduction

With the widespread application of hydraulic energy and the development of water resource engineering, hydraulic machinery, as an indispensable component, plays a crucial role in the hydrodynamic environment [1]. Nonetheless, as a consequence of the substantial sediment content present in natural water, hydraulic machinery inevitably encounters a significant challenge in the form of sediment erosion during its operation [2]. This issue, prominent in the domain of hydraulic machinery, exerts an impact not only on the

performance and longevity of mechanical components [3]. But also carries the potential to jeopardize the efficiency and reliability of hydropower generation [4].

Numerous scholars have conducted comprehensive investigations on the phenomenon of sediment erosion in hydraulic machinery. Noteworthy researchers, such as Finnie [5], Bitter [6], Tilly [7], Sheldon and Kanhere [8], Hutchings [9], and Levy [10], have successively put forth influential and representative erosion mechanisms. These scholars postulate that the erosion behavior of ductile materials is a result of the micro-cutting caused by particle impact on the surface. Consequently, the metal surface of the target material undergoes work hardening, thereby enhancing its strength and reducing the erosion rate. An escalation in collisional stresses during wear leads to the formation of surface cracks on the target material. The impact of particles on friable surfaces results in transverse and radial cracks, respectively, potentially facilitating crack propagation. These surface cracks cause the target material to fragment into smaller pieces, which are subsequently carried away by other impacting particles. Two commonly utilized wall erosion models are available: the Finnie model [5], where the erosion quantity is a function of velocity and attack angle, and the Tabakoff erosion model [11], which incorporates additional solid-phase parameters. Notably, these models have been validated through experimental findings involving Francis turbine components and materials. Teran et al. [12] used the Tabakoff erosion model to analyze turbine erosion conditions and, thus, optimized the operation strategy of power plants. Gautam et al. [13] analyzed the sediment erosion of a low-specific-speed Francis turbine using the Tabakoff erosion model and validated the results by comparing them with the experimental results; the results showed that the degree of erosion was positively correlated with the size of the sediment particles. Thapa B. S. et al. [14] assert that numerous hydropower stations are progressively being established in regions where rivers are subject to sedimentation. The erosion of sediment particles induces alterations in the turbine flow, resulting in efficiency reduction, vibrations, and turbine damage. It has been found that the disruption of the turbine gap, caused by a combination of cross flow and secondary flow, impacts the velocity distribution within the flow channel, thereby intensifying the harmful consequences of sediment erosion on the turbine.

Lu Li et al. [15] conducted an experimental study to examine the wear patterns and wear performance of alternative overflow component materials under specific sediment and overflow conditions related to the Baihetan Power Station's overflow components. They obtained wear depth data for different material surfaces under various sand concentrations and overflow velocities through experiments. Additionally, they derived wear rate equations for different materials by employing a multiple linear regression method. Liu Gongmei et al. [16] estimated sediment wear on the runner blades and guide vanes of hydraulic turbines downstream of the Jinsha River, utilizing empirical equations for sediment wear. However, it was noted that rotating-disk experiments did not sufficiently consider the similarity between the flow field of the specimen and that of the actual hydraulic turbine. Pang [17] conducted a comprehensive numerical simulation of sand–water flow within a high-head Francis turbine using the N-S (Navier–Stokes) equations and the standard $k-\epsilon$ turbulence model. They also performed a single-flow channel sediment erosion test to identify the primary location of sediment abrasion and the degree of damage to the turbine's runner blades. Finally, they established an equation for the abrasion rate of the turbine's runner blades based on their research findings. Thapa B. S. [18] employed experiments and numerical simulations to investigate the vulnerable areas and severity of abrasion that may occur on the guide vanes of a hydraulic turbine within a multi-mud river basin. The most susceptible areas for abrasion were identified, including the fixing bolts of the guide vane, the guide vane's lower anti-erosion plate, and the bottom ring near the guide vane's fixing holes, and potential remedial measures were proposed. Qian Zhongdong et al. [19] performed a sediment erosion analysis on a water pump's blade heads of various shapes and compared them with the wear of the prototype pump impeller. They found that blade wear was influenced by the distribution of water flow velocity and the attack angle. Padhy [20] determined that the size of the sediment particles played a

crucial role in material wear and damage through experimental investigations. Pachón et al. [21] reported that nozzles treated with a plasma nitriding process or anti-erosion material spraying were particularly susceptible to wear. Koirala et al. [22,23] developed a wear model for predicting bucket wear by conducting experiments with different sediment sizes and concentrations, scaling down a power station bucket. Rajkarnikar et al. [24] conducted rotating-disk erosion tests on Francis turbine runner blades, confirming that traditional design methods for runners could lead to sediment erosion on the blade surface and blade damage. Krause et al. [25] studied the impact of sand particle characteristics and content on wear using a test device to simulate the wear flow in a turbine. They identified particle velocity, concentration, hardness, and diameter as the most influential factors affecting a material's wear rate. Poudel et al. [26] investigated the impact of sediment particles of various shapes and sizes on the wear of turbine flow-passing components using high-speed test rigs and a rotating-disk apparatus (RDA). Padhy et al. [27] established relationships between sand particle size, sediment volume fraction, and erosion rate through experiments on small bucket turbines. Kenichi et al. [28] explored the effects of the attack angle and a material's hardness on wear through jet wear tests on a range of materials and coatings. By using the Euler–Lagrange method, Liu [29] and Huang [30] studied the sediment wear mechanism of the flow parts of the impact turbine and found that the sediment speed caused severe wear and erosion on the jet mechanism and the bottom of the bucket blade of the impact turbine from the perspective of sediment concentration and the operating conditions. At the same time, Deng [31] found that the jetting needle of the impact turbine was offset after wear, causing the jet water to be unable to uniformly shoot into the bucket, resulting in unbalanced radial and axial forces on the impact turbine runner, and the unit stability decreased.

With the rapid development of computational fluid dynamics (CFD), CFD technology has been gradually applied to simulate the flow field inside the solid–liquid two-phase flow of fluid machinery. Koirala [32] conducted an investigation into the impact of the degree of wear of the guide vane end gap on the overall performance of a Francis turbine within a hydropower station. They correlated their initial findings with an empirical relation equation predicting leakage flow. Furthermore, they introduced a method for calculating the wear depth. Noon [33] and Neopane [34] pointed out that the sediment wear of hydraulic turbine components is generally influenced by factors such as sediment particle concentration, size, shape, flow velocity, rotor material properties, and operating hours. This wear leads to alterations in the geometrical shape of the rotor components, resulting in a decrease in hydraulic efficiency. Messa [35] employed the VOF model to simulate the nozzle jet of a bucket turbine and utilized a Lagrangian particle-tracking model to replicate the trajectory of solid particles. Leguizamon [36] proposed a multiscale wear model suitable for investigating sediment wear in hydraulic turbines.

In recent years, researchers and scholars have recognized that the existing wear models only provide wear rate information at the initial boundary. To improve wear prediction and account for the pit morphology on overflow walls caused by wear, Chen et al. [37] introduced a stochastic rebound model for predicting both the wear rate and the wear morphology of a tee. Mansouri [38] employed computational fluid dynamics (CFD) simulations to characterize the velocity, angle, and frequency of particle impacts at specific locations within a specimen. They then correlated this particle impact data with the measured wear depth to derive wear equations for impact wear experiments. Messa [39] proposed a wear prediction model based on the Eulerian model for particle trajectories and wear morphology. In this model, the flow field was calculated as a constant simulation, and the trajectories of individual particles near the solid wall were repeatedly computed to obtain a continuously updated Bahrainian [40] model. This was achieved through a novel nonlinear approach based on the Gaussian process regression (GPR) method, enabling the prediction of wear on the wall caused by solid particles. Dong [41] developed a wear prediction method using the discrete element method (DEM), which considers cutting and

deformation mechanisms. Empirical coefficients were introduced to establish a correlation between the wear rate and the wear volume.

This study focused on the design of a sediment abrasion test device for the water diversion mechanism of a low-head power station situated in the Dadu River basin, China. To achieve this, the Euler–Lagrange method was employed for the numerical simulation, allowing for the analysis of the sand–water flow characteristics within the power station’s water-guiding components. By conducting this simulation, characteristic parameters pertaining to the sediment particle flow within these components were obtained. Taking into consideration the operational principles of the hydraulic turbine’s water-guiding mechanism and adhering to the similarity principle governing flow fields, three distinct single-channel sediment particle bypass wear test devices for water-guiding mechanisms were formulated. Subsequently, the sand–water flow field of these test devices was subjected to simulation and analysis, enabling a comparison with the flow field within the actual water-guiding components of the machinery. The research results are helpful for accurately carrying out sediment wear tests of the water-guiding mechanism and further analyzing the sand and water flow characteristics and wear mechanism on the surface of the guide vane.

2. Numerical Simulation

2.1. Power Station Parameters

This study is centered around the water-guide mechanism of a low-head power station situated in the Dadu River basin, China. Notably, the Dadu River basin serves as the source of sediment for the Minjiang River, exhibiting a multiyear average sand content of 0.475 kg/m³ and an annual sand transport of 22.47 million tons. The upstream watershed of the power station spans an area of 76,130 km², featuring a multiyear average annual runoff of 47.25 billion m³ and an average flow rate of 1500 m³/s. The majority of sediment from the power station is primarily concentrated between May and October each year, with a multiyear average annual sand delivery of 29.9 million tons. The measured sand content varies, with a maximum of 27.6 kg/m³ and a minimum of 1.5 kg/m³, while the average grain size falls within the range of 0.098–0.131 mm, with the largest particle size measuring 2.7 mm.

The power plant primarily comprises overflow components, including a worm shell, seat ring, a guide vane, a runner, and a tailpipe. The specific operational parameters of the power plant can be found in Table 1.

Table 1. Design and operation parameters of a reaction hydraulic turbine.

| Parameter | Value | Parameter | Value |
|--|-------|----------------------------------|-------|
| Head H (m) | 44 | Stay vane | 22 |
| Power P (MW) | 112.6 | Guide vane | 24 |
| Rotational speed n (r/min) | 88.2 | Vane height (m) | 1.375 |
| Design flow rate Q (m ³ /s) | 290 | Distribution circle diameter (m) | 6.5 |
| Runner diameter D ₁ (m) | 5.9 | Number of runner blades | 13 |

The specific rotational speed is a vital comprehensive parameter in hydraulic turbines, serving as an indicator of the overall performance of a set of hydraulic turbines operating under similar working conditions. This parameter is valuable for classifying fluid machinery, establishing serial designs, and facilitating similar design processes. The specific speed of a hydraulic turbine offers insights into critical unit characteristics, including water flow energy, cavitation performance, and geometric parameters. The formula for calculating the specific speed of the hydraulic turbine in this power station is as follows:

$$n_s = \frac{n\sqrt{P}}{H^{5/4}} \tag{1}$$

where n is the rotational speed, r/min; P is the rated output of the hydraulic turbine, kW; and H is the rated head, m.

The specific rotational speed of the plant, calculated to be 261.22, indicates that it is a medium–high specific rotational speed mixed-flow turbine. This implies that, when the unit's flow rate is substantial, the height of the guide apparatus is high, and the impulse angle of the water flow at the inlet of the guide vane is approximately zero.

2.2. Three-Dimensional Model and Meshing of the Guide Apparatus

2.2.1. Three-Dimensional Model

In this study, the primary focus is on simulating the characteristics of sand and water flow within the overflow components of the power station. An overflow water body model is established, including components such as the power station's snail shell, the stay vane, and the guide vane, as illustrated in Figure 1.

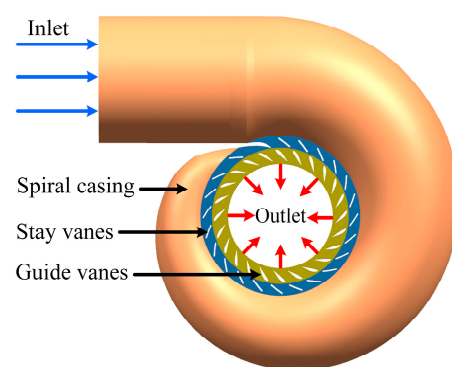


Figure 1. Three-dimensional water area model of the diversion parts of a hydropower station.

2.2.2. Mesh Segmentation and Independence Verification

This study employed the CFX for the numerical simulation calculations, emphasizing the importance of mesh quality in achieving accurate calculation results. A fluent meshing software was utilized to create meshes for the water body model of the water diversion components. Unstructured meshing was employed for the water body, particularly for the complex structure of the snail shell and the water-guiding mechanism. Additionally, a smaller mesh size was applied to the tongue region of the snail shell, and mesh refinement techniques were used on the wall surface of the snail shell and the tongue region. Ultimately, a hexahedral mesh configuration was employed as the mesh model for the numerical calculations. As shown in Figure 2.

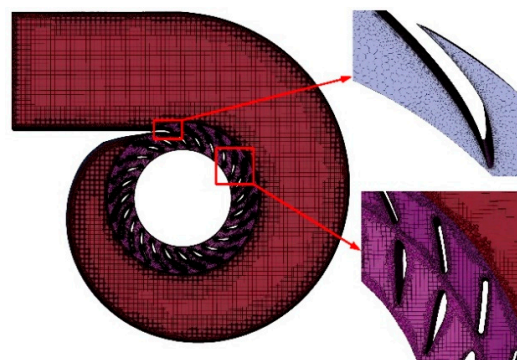


Figure 2. Mesh model of the water area for the diversion parts of a hydropower station.

Furthermore, to mitigate the impact of mesh count on the accuracy of the numerical calculation results, this study divided the mesh into five sets with varying numbers of mesh elements. The mesh parameters of each group are shown in Table 2. The specific

mesh parameters for each set are detailed in the table provided. Mesh quality typically falls within the range of 0 to 1, while the mesh aspect ratio ranges from 0 to 100. Higher values approaching 1 for mesh quality indicate a better mesh quality. In general, for numerical simulations, the mesh quality should exceed 0.2.

Table 2. Mesh independence verification.

| Mesh | Number of Mesh ($\times 10^4$) | | | Mesh Nodes ($\times 10^4$) | Min Mesh Quality (0~1) | Mesh Size (Length \times Width) (mm) |
|------|----------------------------------|------------|-------------|------------------------------|------------------------|--|
| | Spiral Casing | Stay Vanes | Guide Vanes | | | |
| 1 | 190.4 | 173.9 | 82.4 | 492.7 | 0.06 | 5.76×0.3 |
| 2 | 297.2 | 241.4 | 151 | 728.1 | 0.11 | 4.23×0.3 |
| 3 | 388.7 | 302.6 | 221.9 | 992.4 | 0.24 | 2.7×0.3 |
| 4 | 468.6 | 390 | 300.8 | 1285.8 | 0.43 | 3.3×0.2 |
| 5 | 545.7 | 462.8 | 402.3 | 1598.6 | 0.46 | 1.18×0.2 |

The sand–water bypass velocity near the wall on the backside of the stay vane was used as a judgment target to determine the mesh model for the numerical calculations. Finally, Mesh 4 was chosen as the mesh model of the computing domain. The mesh division irrelevance verification is depicted in Figure 3.

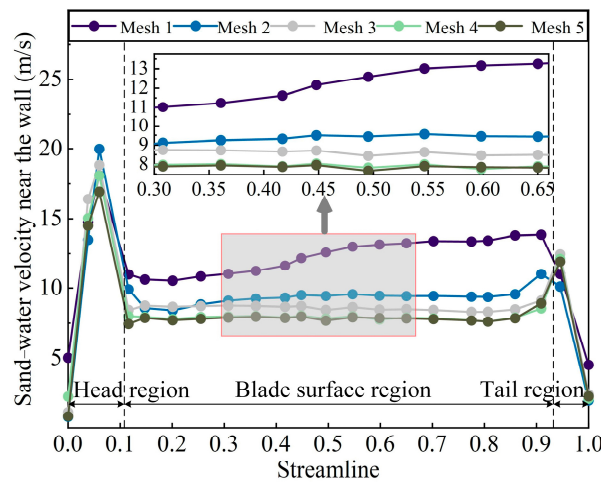


Figure 3. Mesh independence verification.

2.3. Mathematical Model

2.3.1. Basic Control Equations

In this study, water was assumed to be an incompressible fluid, treated as a continuous phase. The flow behavior was described within the Eulerian coordinate system, and the governing equations were the standard unsteady flow control equations [42]. These equations were solved using the Navier–Stokes equations—the continuity equation and the momentum equation—which were expressed as follows:

$$\frac{\partial \rho}{\partial t} + \frac{\partial}{\partial x_i}(\rho u_i) = 0 \tag{2}$$

$$\rho \left(\frac{\partial u}{\partial t} + u_i \frac{\partial u_j}{\partial x_i} \right) = -\frac{\partial p}{\partial x_i} + \mu \frac{\partial^2 u_i}{\partial u_i \partial u_j} + \left(\frac{1}{3} \mu + \mu_t \right) \frac{\partial}{\partial x_i} \left(\frac{\partial u_i}{\partial x_j} \right) + f_i \tag{3}$$

where ρ denotes the fluid density, kg/m^3 ; u denotes the velocity, m/s ; t denotes the time; p denotes the pressure, pa ; μ denotes the fluid viscosity coefficient, $\text{pa}\cdot\text{s}$; and f_i denotes the force acting on the fluid.

2.3.2. Turbulence Model

In this study, the standard $k-\epsilon$ turbulence model was used with the turbulent kinetic energy k equation and the dissipation rate ϵ equation:

$$\frac{\partial}{\partial t}(\rho k) + \frac{\partial}{\partial x_j}(\rho k u_j) = \frac{\partial}{\partial x_j} \left[\left(\mu + \frac{\mu_t}{\sigma_k} \right) \frac{\partial k}{\partial x_j} \right] + G_k + G_B - \rho \epsilon + Y_m \quad (4)$$

$$\frac{\partial}{\partial t}(\rho \epsilon) + \frac{\partial}{\partial x_i}(\rho \epsilon u_i) = \frac{\partial}{\partial x_j} \left[\left(\mu + \frac{\mu_t}{\sigma_\epsilon} \right) \frac{\partial \epsilon}{\partial x_j} \right] + C_{1\epsilon}(G_k + C_{3\epsilon}G_B) \frac{\epsilon}{k} - C_{2\epsilon} \rho \frac{\epsilon^2}{k} \quad (5)$$

where $C_{1\epsilon}$, $C_{2\epsilon}$, and $C_{3\epsilon}$ are empirical constants; σ_k and σ_ϵ are the Prandtl numbers related to the turbulent kinetic energy k and the dissipation rate ϵ , respectively; G_k represents the turbulent kinetic energy due to the mean velocity gradient; G_B represents the turbulent kinetic energy due to buoyancy; μ_t represents the turbulence viscosity coefficient; and Y_m represents the effect of pulsating expansion in compressible turbulence on the total dissipation rate [43].

2.3.3. Calculation of the Boundary Conditions

Based on the statistical analysis of the power plant’s operating logs, it was determined that the power plant operated under rated conditions for approximately 90% of the total operating time. Therefore, the primary objective of this study was to calculate the sand and water flow within the unit’s flow field under these rated operating conditions. Additionally, it was noted that the rated degree of opening for the guide vane was 40° , as shown in Figure 4.

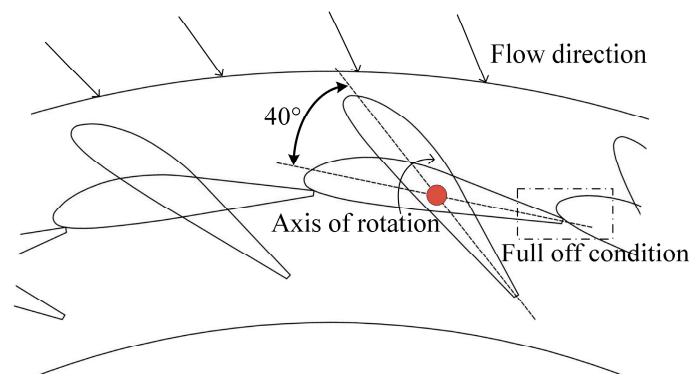


Figure 4. Diagram of guide vane opening.

A numerical simulation’s boundary conditions are fundamental for accurate numerical calculations. In this study, the volume of sediment particles α_s was set to 0.00189, corresponding to a sediment concentration of 5 kg/m^3 . Additionally, the sand–water density ρ_{s-w} was calculated as follows:

$$\rho_{s-w} = \frac{\rho_s \alpha_s + (1 - \alpha_s) \rho_w}{V_{s-w}} \quad (6)$$

where α_s is the volume fraction of the sediment particle phase; ρ_s is the density of the sediment particle phase, which was 2650 kg/m^3 ; ρ_w is the density of the water phase, with a value of 998.2 kg/m^3 ; and V_{s-w} is the volume of the sand and water, set to 1 m^3 .

Regarding the boundary conditions used in the numerical simulation, the inlet boundary condition, with the worm shell as the inlet, was defined as a mass flow inlet, with a specified value of $290,380.77 \text{ kg/s}$. The velocity near the wall needed to satisfy the no-slip wall condition. Therefore, the standard wall function was applied in the near-wall region. The outlet boundary condition was applied on the guide vane’s outlet circular surface, and

it was set as a hydrostatic outlet. The calculation of the hydrostatic outlet p_2 was based on Bernoulli's equation.

$$\frac{p_1}{\gamma} + \frac{v_1^2}{2g} + z_1 = \frac{p_2}{\gamma} + \frac{v_2^2}{2g} + z_2 + \Delta h \tag{7}$$

where p_1 and p_2 represent the pressure on the circular surface of the inlet of the worm shell and the outlet of the guide vane, respectively; v_1 and v_2 represent the velocity at the circular surface of the inlet of the worm shell and the outlet of the guide vane, respectively, m/s; γ represents the gravity of the sand and water, N/m³; z_1 and z_2 represent the positional heights of the circular surfaces of the inlet of the worm shell and the outlet of the guide vane, respectively, m; and Δh is the hydraulic loss, with a specified value of 0.44 (0.01 H), m.

3. Design of Flow-Around Erosion Test

3.1. Velocity Triangle of the Guide Apparatus

The hydraulic turbine guide apparatus plays a crucial role in the hydro generator unit, as it controls the direction and magnitude of water flow into the unit during its operation. Its proper functioning is essential for the stability and safety of the entire unit operation. This mechanism primarily comprises two types of wing structures: stay vanes and guide vanes. Generally, the stay vane does not alter the flow volume of water in the worm shell, and its wingbone line pattern extends from the equiangular screw line in the worm shell. Depending on changes in the power system's load, the opening degree of the guide vane is adjusted to regulate the turbine flow rate, aligning it with the system requirements for the unit output. This adjustment modifies the water flow annulus entering the runner to meet the turbine's specific needs.

Figure 5 illustrates the velocity triangle inside the guide apparatus, which reflects the characteristics of two-phase flow motion in the sand-laden water flow field of the guide apparatus. In this study, the analysis focuses on the stay vane inlet velocity triangle, and the law of conservation of velocity moments is applied at all points within the guide apparatus. The similarity between the stay vane's inlet and outlet velocity triangles is significant, with α_{G0} and β_{G0} varying under different working conditions, resulting in different velocity triangles. These variations ultimately regulate the unit's flow rate. The fundamental equation for velocity moments is as follows:

$$\frac{Hg\eta_s}{\omega} = V_{Su0}r_0 = V_{Su1}r_1 = V_{Gu0}r_2 = V_{Gu1}r_3 \tag{8}$$

where V , U , and W are the absolute, circumferential, and relative velocities, respectively; H is the operating head of the turbine, m; g is the local gravitational acceleration, m/s²; η_s is the hydraulic efficiency of the guide vane, which can be approximated to 1; α and β are the inlet angle and the exit angle of the guide vane, respectively; S and G refer to the stay vane and the guide vane, respectively; 0 and 1 correspond to the inlet and exit of the guide vane, respectively; and r_0 , r_1 , r_2 , and r_3 are the distributing circular radii of the guide vane's inlet and outlet, respectively.

3.2. Principles of Design for Flow-Around Erosion Tests

Numerical simulations of the sand and water flow in the hydraulic turbine under test conditions were conducted to obtain information on the sand and water velocities, the streamline distribution, and the sediment concentration distribution on the guide vane's surface. This guide vane served as the path for bypassing the wear test. Subsequently, a test device was designed, and the wear test was performed. The test model's design closely mimicked the flow conditions of the actual flow channel, ensuring that the test results aligned with real-world outcomes.

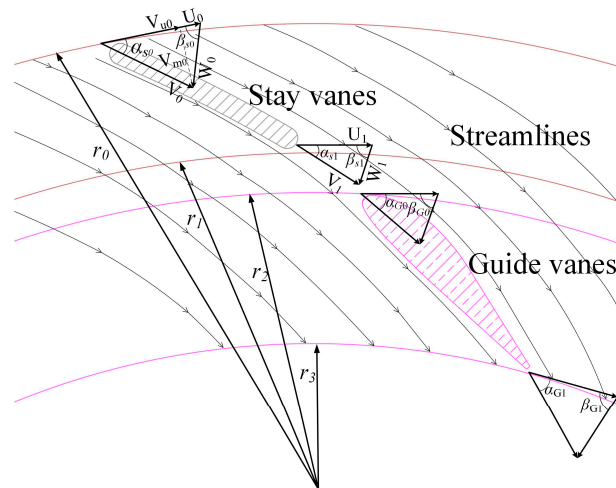


Figure 5. Velocity triangle of the distributor.

The test design flow path, as shown in Figure 6a, was derived from the actual sandy water flow path within the diversion component. The shape of this flow path generally conforms to the equiangular solenoidal equation of the worm shell design. This suggests that the velocity loop characteristics of the sandy water flow within the diversion component remain relatively stable during flow, with relatively low hydraulic losses within the diversion component. The winding wear test flow path, depicted in Figure 6b, was designed based on the sand–water flow patterns under the rated operating conditions of the unit. The inclusion of both stay vanes and movable guide vanes in this design helped prevent the sand–water flow near a single guide vane from being influenced by the adjacent wall.

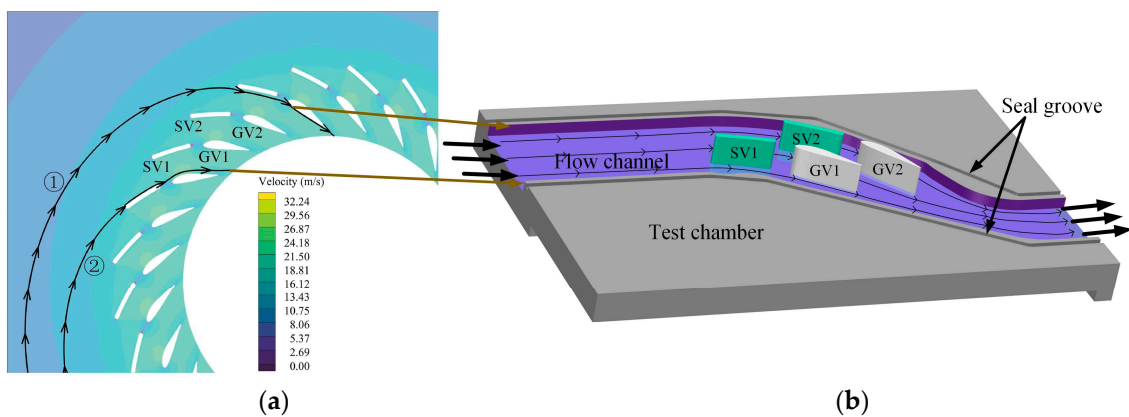


Figure 6. Design principle of the sediment erosion test around the flow. (a) Sand–water streamlines of distributor; and (b) test device design diagram.

Within a certain range of test system pressures, sandy water flowed around the surface of the guide vane specimen, causing the specimen to be abraded by the cutting or impact of sediment particles. Based on the sandy water flow pattern depicted in Figure 6a a guide apparatus was designed to bypass the flow and wear test device. The test device’s design included two sets of guide vanes positioned in the middle of flow lines ① and ②. To ensure that the test device was geometrically similar to the guide apparatus of the actual machinery and that the sandy water flow conditions (velocity magnitude, direction, and distribution of sand particles) inside the test device remained consistent, the guide vanes were scaled up and down in proportion. This ensured that the test system could handle the water transfer capacity and adhere to the sandy water velocity limitations of the unit’s operating conditions.

3.3. Design of the Test Device System

The sediment wear-bypassing test system for the guide apparatus comprised four main components: a test device, a cooling system, a mixing system for sand and water, and a power system, as illustrated in Figure 7. The test device included a guide vane specimen, a test chamber, and a makeup air device. The configuration of the flow channel within the test chamber was determined based on the flow field characteristics under various working conditions. It was observed that high flow rates at the exit of the flow channel in the test chamber were susceptible to cavitation. To address this issue, a makeup air device was installed at the exit of the test chamber to equalize the pressure within the inner flow channel with the atmospheric pressure. The power system consisted of a multistage centrifugal pump and a motor. The motor had a maximum power rating of 630 kW. The multistage centrifugal pump was designed with a rated flow rate of 280 m³/h and a head of 376 m. The cooling system was arranged in the sand–water mixing tank serpentine pipe cold water internal circulation device and cold water was added in the serpentine pipe section circulation flow so that the sand–water mixing system could stay cool. The capacity of the sand–water mixing system was 15 m³, and two methods of water impact and mixing were adopted to mix the sand particles and water evenly. A stainless steel water pipe with a diameter of 200 mm was used for the test pipeline.

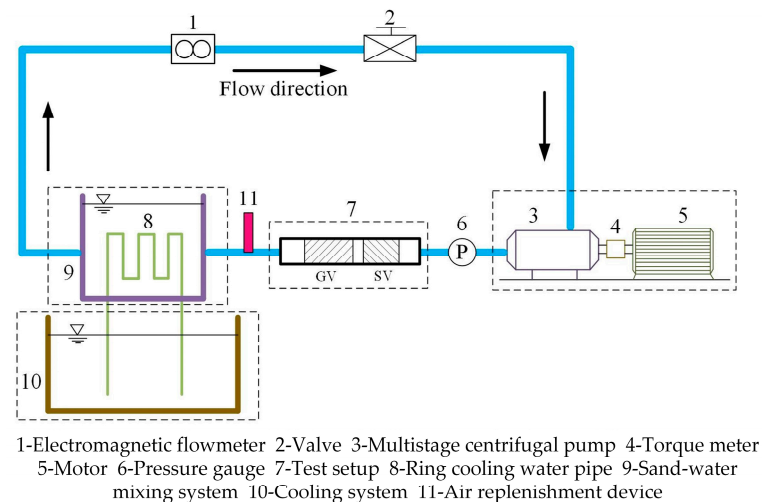


Figure 7. Sediment erosion around the flow test system.

4. Analysis of the Numerical Simulation Results of the Test Device

4.1. Analysis of Sand–Water Flow in the Guide Apparatus

Figure 8a,b illustrate the numerical simulation results of the pressure distribution and velocity distribution, respectively, within the power station diversion components. These results reveal that, as sandy water progressed from the inlet of the worm shell to the outlet of the movable guide vane, the overflow area progressively diminished, causing the pressure potential energy of the sandy water flow to gradually convert into velocity potential energy. The snail shell caused the sandy water to flow into a ring; the internal flow showed an axisymmetric potential flow trend; and the velocity at each point was approximately constant. The maximum pressure occurred at the inlet of the worm shell, and the internal pressure change in the water diversion components was in line with the design principle of power plants' hydraulic machinery.

The sediment particle velocity was the main factor influencing hydromechanical structure wear and erosion damage. In the water-guide mechanism, sediment particles were affected by the force of the water flow and by the high-speed water flow hostage movement to the runner, through which the guide vane near the wall surface of the sediment particle velocity approached the water flow velocity. The velocity of the sediment particles and the abrasion of the surface of the overflow components usually exhibit an exponential

growth trend; the maximum flow velocity inside the water-guiding components occurred at the outlet end of the movable guide vane, with a maximum sand–water velocity of 32.24 m/s, and the sand–water velocity on the near-wall surface of the guide vane was uniformly distributed.

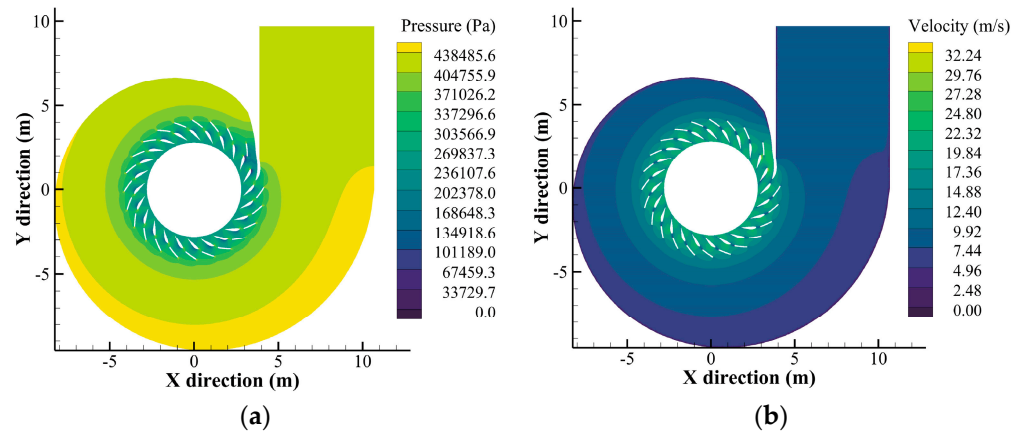


Figure 8. Distribution of the flow field of the distributor. (a) Pressure distribution of the distributor and (b) sediment velocity distribution of the distributor.

Figure 9 presents the distribution of sand and water streamlines within the water diversion component, as well as the distribution of vortex volume within the guiding apparatus. The relationship between sand streamlines and the trajectories of sediment particles in the hydraulic turbine is intricate and subject to variation. In high-concentration sand–water, mutual collisions among sediment particles affect their trajectories, while, in low-concentration sand–water, the collision behavior among sediment particles can be disregarded. In such cases, the primary forces acting on the sediment particles are the drag force and the gravitational force. Therefore, the sand–water streamlines studied here can effectively represent the motion trajectories of sediment particles inside diversion components. The motion trajectories of the sediment particles within the diversion components appear uniform and smooth, with low flow velocities and no evident reflux or secondary flow phenomena.

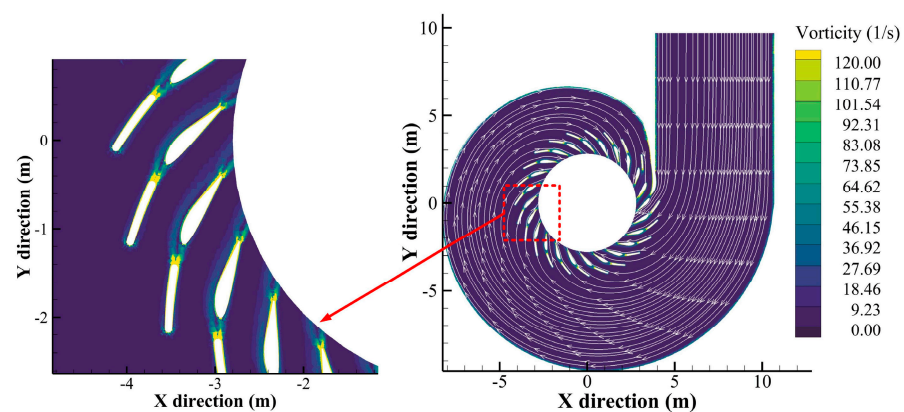


Figure 9. Vorticity and streamline distribution of the distributor.

Over time, the sediment particles within the vortex region and those on the surface of the guide vane undergo changes. As a result, the sediment particles on the surface of the structure downstream of the vortex region experience more collisions, leading to an increased number of impacts on the structure. Consequently, the wear phenomenon on the overflow components becomes more pronounced. Figure 10 illustrates the sediment wear phenomenon on the head of the movable guide vane in the power station and the head of

the test bench specimen. It is evident that the impact wear caused by the sediment particles on the head is significantly more substantial than that on the surface of the guide vane.

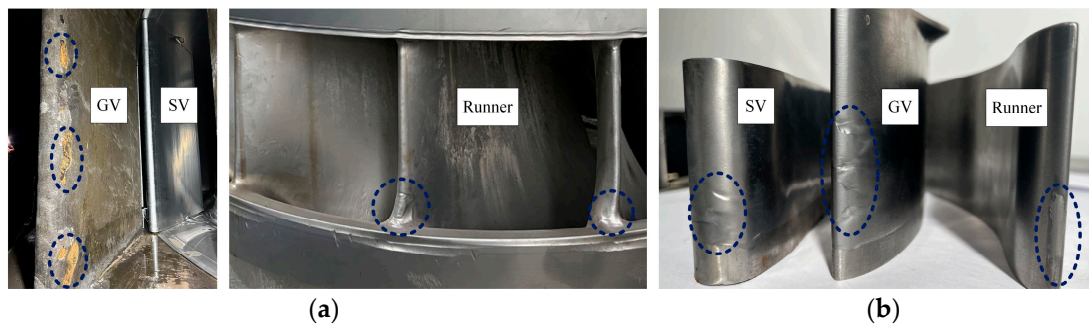


Figure 10. Head erosion phenomenon of the flow sections. (a) Prototype hydraulic turbine structural components; and (b) test specimen.

4.2. Analysis of the Sand Flow in the Test Device

Figure 11 provides the results of the calculated pressure and velocity distribution within the flow field of the test device. Notably, the front side of the guide vane within the test device exhibits a uniform pressure distribution, with the pressure at the test outlet reaching its maximum due to the gradual reduction in the flow channel overflow area, as determined by the test design principle. In the head area at the back of the guide vane, there is a significant pressure gradient, with the gradient diminishing along the flow direction. This pressure distribution at the front and back of the guide vane aligns with the trend of pressure distribution and pressure gradient changes within the guide apparatus of the actual power station unit.

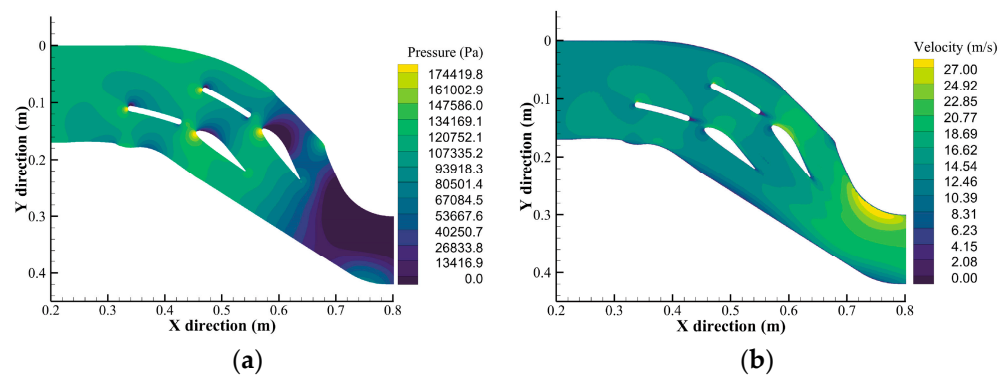


Figure 11. Distribution of the flow field of the test device. (a) Pressure distribution of the test device and (b) sediment velocity distribution of the test device.

When considering the wear and tear of a test specimen, sand and water velocity are typically important factors. In this case, the inlet sand and water velocities of the test device were determined based on the sand and water velocity in the test pipe, and the inlet flow velocity of the test section was established according to the test conditions. Along the same overflow surface, the front side of the guide vane exhibited a slightly higher flow velocity compared to the back side, with the maximum flow velocity occurring at the test outlet, reaching a maximum sand and water velocity of 27 m/s. Notably, the stay vane’s tail section featured a significant local low-velocity area. This was due to the tail section being a large-diameter circular structure, where the sand velocity neared a stationary velocity, resulting in a substantial stationary-velocity area. This disturbance in the sand and water flow state within the leafless area between the tail of the stay vane and the head of the movable guide vane led to noticeable sediment abrasion erosion on the head of the movable guide vane. In contrast, the movable guide vane had an airfoil

structure with positive curvature, and the circular transition structure at its tail had a smaller diameter. Consequently, the stationary area of the sand and water velocity was lower, and the turbulence caused by sand and water at the tail had a less pronounced impact on the flow at the test outlet. In conclusion, the distribution of the internal flow field within the test device closely mirrored the internal flow field state within the guide apparatus of the actual power station unit. This high degree of accuracy in the test device allowed it to completely represent the phenomenon of sand–water flow within the real power station.

Figure 12 displays the distribution of vorticity and the sand–water flow lines within the test device. Here are the key observations: in the leafless area between the front end of the stay vane and the guide vane in the prototype unit of the power station, the sand and water flow state is not constrained by the wall. Consequently, the vortex strength of the guide vane wall is small. In contrast, the wall of the test runner exerts stronger constraints on the sand and water flow, leading to a larger vortex strength. At the tail of the stay vane, there is a noticeable high-intensity vortex area, while the tail of the movable guide vane exhibits a smaller vortex area. The sand and water flow within the test runner is smooth and uniform. The sand particles flow forward along the runner, from the head of the guide vane, creating a bypassing state for the guide vane. The sand and water flow within the test section does not exhibit obvious reflux or secondary flow phenomena. The local vortex generated by the sand and water flow at the tail of the guide vane primarily impacts the abrasion and erosion of the head of the next level of overflow components. Importantly, the sand-and-water-bypassing state on the surface of the guide vane remains unaffected by the vortex at the tail of the guide vane.

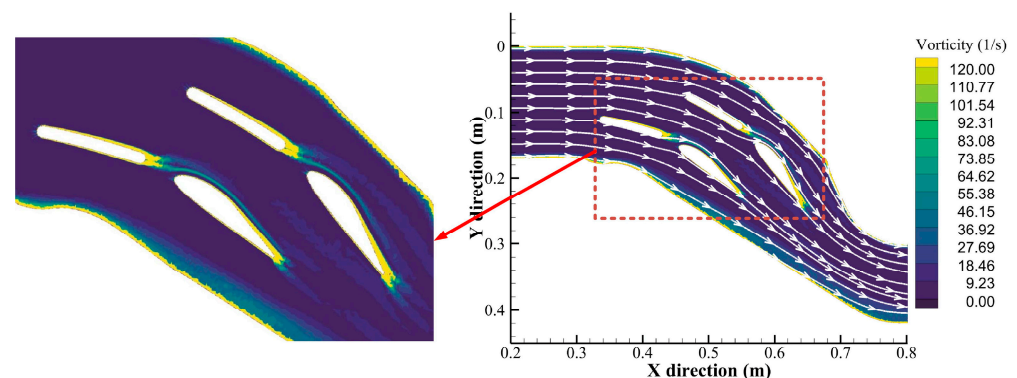


Figure 12. Vorticity and streamline distribution of the test device.

The results of the flow field analysis inside the test device showed that the results of the single-runner bypassing wear test design were in line with the sand and water flow states inside the water-guide mechanism of the prototype unit, which provided greater accuracy for exploring the sediment wear phenomenon of the key overflow components of the water-guiding mechanism. The test set completely explored the microscopic wear process of sediment particles on the structure and revealed the sediment wear mechanism and law.

4.3. Comparative Analysis of Test Device Accuracy

Figure 13 illustrates the distributions of sand and water velocities on the near-wall surface of the stay vane of the real machine at the power station and the stay vane of the test device. Here are the key observations: The stay vane is a symmetric wing structure with a uniform thickness, and the near-wall sand and water velocities at the front and back of the guide vane change uniformly without obvious gradients. In the head region of the stay vane in the test device, the near-wall sand and water velocities reach a maximum of 24.5 m/s, while the corresponding velocities in the same position in the prototype set are approximately 13.4 m/s. The significant difference in the sand and water velocities at the head of the guide vane between the test device and the prototype set is due to

the constraints on the front end of the stay vane in the test device from the flow channel wall surface. In contrast, the prototype set is located inside the worm shell, resulting in a different velocity profile at the head of the guide vane. Despite the differences in the sand and water velocities at the head of the guide vane, the flow trends of sand and water in the head of both water-guide mechanisms are the same, with a uniform and smooth flow. At the tail of the stay vane, the flow of sand and water is disrupted by the structure of the guide vane, leading to the formation of two symmetric vortices with varying strengths. This results in step and plunge phenomena in the sand and water velocity at the tail of the guide vane. The head and tail of the stay vane experience significant changes in the sand and water velocities, and these positions are the most severely affected by sediment abrasion-related erosion damage. Sediment particles are influenced by the vortex field, leading to secondary flow and reflux phenomena at the tail of the guide vane, which, in turn, impact the temporal characteristics of sediment abrasion and erosion. The head and tail of the guide vane's structural surface are subjected to severe abrasion and erosion, resulting in more significant damage in these areas. These findings provide valuable insights into the differences in the sand and water velocities and erosion characteristics between the test device and the real machine in the power station, particularly at the head and tail of the stay vane.

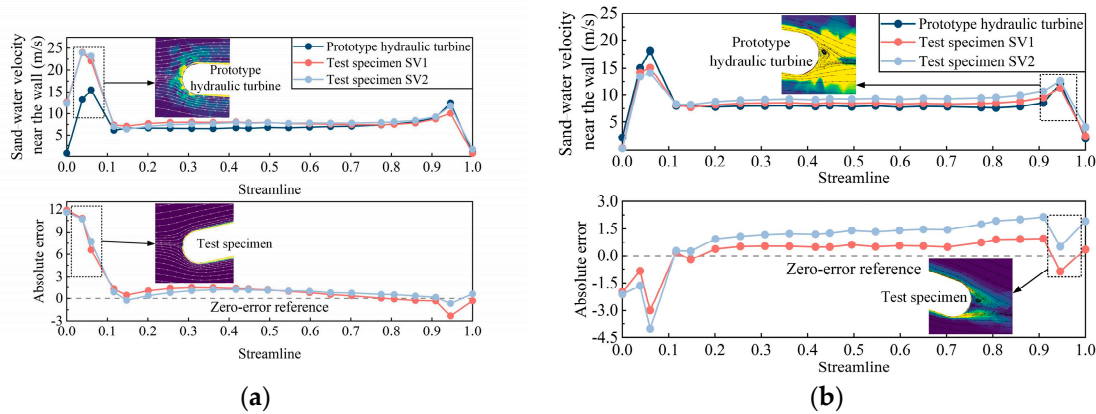


Figure 13. Sand–water velocity distribution near the wall of the stay vane. (a) SV pressure side; and (b) SV suction side.

Figure 14 illustrates the distributions of the sand and water velocities on the near-wall surface of the guide vane of the real machine at the power station and the guide vane of the test device. The near-wall sand and water velocity distributions of the front and back of the active guide vane in the test device are consistent with those of the prototype set, and the near-wall sand and water velocities at the head of the active guide vane are the largest. With the downward flow of sand and water along the flow channel, the velocity of sand and water on the front side of the movable guide vane gradually decreases. A small velocity gradient is observed on the back side of the movable guide vane. The difference between the near-wall velocity of sand and water on the back side of the movable guide vane of the prototype set and that on the back side of the guide vane of the experimental device remains within 1 m/s. Additionally, the difference in the near-wall velocity of sand and water on the front side of the guide vane is within 3 m/s. The flow separation phenomenon at the head of the movable guide vane and the reflux phenomenon of the sand and water at the tail create a local “high-speed zone” of sand and water at both ends of the guide vane. It is noteworthy that the flow separation phenomenon of the sand and water is more likely to result in a sharp increase in the speed of the sand and water compared to the phenomenon of sand and water reflux.

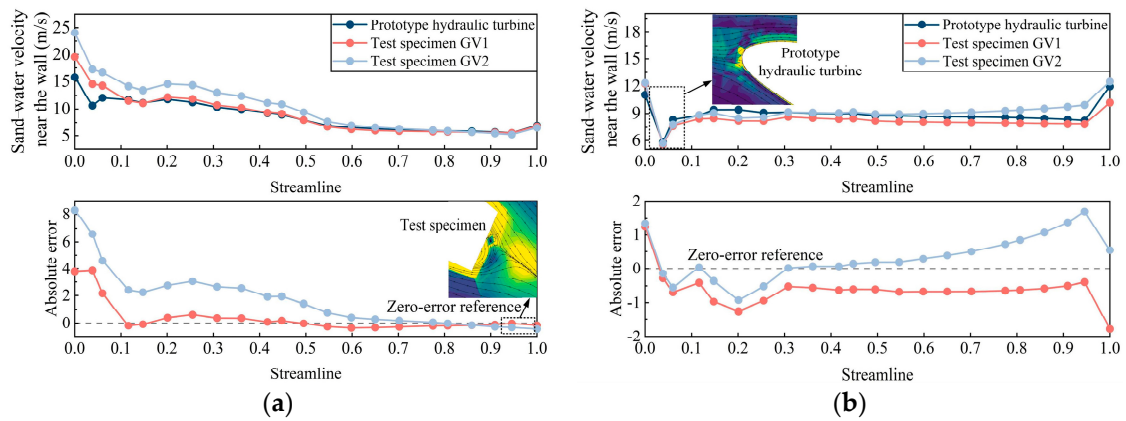


Figure 14. Sand–water velocity distribution near the wall of the guide vane. (a) GV pressure side; and (b) GV suction side.

The calculated results of the surface test device within the stay vane sand and the water flow field distribution were in agreement with the prototype set of stay vane sand and water flow field distribution. The absolute error range of the sand and water near-wall velocity was minimal, confirming that the test device design adhered to the principle of flow similarity.

4.4. Manufacturing of the Test Device

Figure 15 shows the sediment erosion-bypassing test system. The flow erosion test device of the guide apparatus was assembled by the upper cover plate and the lower cover plate. The flow channel contained two sets of stay blades and guide blades. Two positioning pins were installed on the lower cover plate to ensure the compact installation of the two cover plates. The sealing strip ensured that the sand–water contained in the flow channel would not leak, and the flow state inside the flow channel was stable.

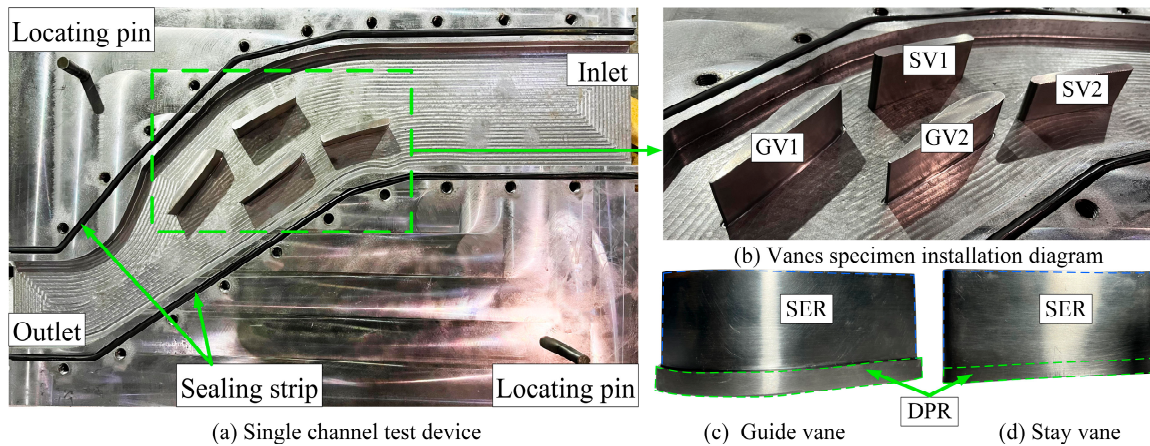


Figure 15. Single-channel test device of the guide apparatus.

The guide vane test specimen material was determined according to the research object. In this study, the stay vane material was 15 MnMoVCu, and the active guide vane material adopted was cast steel ZG06Cr16Ni5Mo. The guide vane specimen adopted a numerical control process to carry out precise processing; the guide vane and the box body adopted sealing to match the installation; the installation gap needed to ensure that the gap was less than 0.1 mm; and the test box body adopted the metal material. The surface roughness of the guide vane specimen met the smoothness requirement of the structure of the guide apparatus in the power station and ensured that the results of the wear test would not be affected by the surface roughness of the guide vane. The surfaces of the

stay vane and the guide vane were divided into a sediment erosion region (SER) and a datum plane region (DPR). The SER was the sediment erosion region around the guide vane surface, and the DPR was the uneroded region. It was the measurement basis of the guide vane specimen before and after wear.

5. Conclusions

This paper presents the design of a single-runner bypassing wear test device for the impact water-guide mechanism and a comparative analysis of the differences in the sand and water flow within the water-guiding components of the prototype unit and the single-runner bypassing wear test device. The primary conclusions are as follows:

1. Based on the triangular velocity transformation of the guide apparatus and the principle of flow similarity, a single-flow channel winding wear test device for the guide apparatus of a hydraulic turbine was designed, and a single-flow channel winding wear test system was used to simulate the solid–liquid two-phase flow in the flow field inside the test device. The numerical simulation of the sand and water flow in the prototype set and test device was carried out by the CFD software.

2. The distributions of the sand and water flow fields in the stay vane and movable guide vane in the test device were consistent with the distributions of the sand and water flow fields in the water-guide mechanism of the prototype unit, and the trends of the changes in the sand and water velocities on the near-wall surface of the guide vane were consistent. Moreover, the flow separation phenomenon at the head of the guide vane and the phenomenon of sand and water reflux at the tail led to the creation of a localized “high-speed zone” in the sand and water velocity along the near-wall surface. The local velocities of the stay vane head in the test device and prototype set were 13.4 m/s and 24.5 m/s, respectively. Additionally, the presence of a vortex at the tail exacerbated the erosion and damage caused by sediment abrasion. This vortex at the tail intensified the erosion and damage of sediment abrasion on the head of the lower-level overflow components. The trailing vorticity of the guide vane reached a maximum of 120 s^{-1} .

3. The wall surface of the test device induced minor fluctuations in the sand and water velocities near the wall surface of the guide vane, and the absolute error range of the sand and water velocities near the wall surface of the guide vane complied with the test device’s design specifications. The velocity of the sediment particles on the surface of the guide vane in the single-channel sediment wear test device and prototype unit ranged from 6.2 to 7.8 m/s, and the velocity of the sediment particles on the surface of the stay vane ranged from 5.1 to 14.6 m/s, and the difference in the sediment particles’ velocity near the wall was 1 to 3 m/s. The single-flow channel sediment abrasion test device was capable of elucidating the sediment abrasion and erosion mechanism of the counterattack hydraulic turbine’s water-guide mechanism.

4. The design principle of the single-channel sediment wear test device of the reaction hydraulic turbine water-guide mechanism followed the flow field similarity principle. In the future, the wear mechanism of the guide vane in different power stations can be revealed, and the operating life of the guide vane can be predicted with the help of this test equipment.

Author Contributions: J.P., X.L., X.C., Y.G., W.X. and Z.Z. proposed the simulation method and designed the experiment; J.P., X.C. and Y.G. completed the numerical simulations; J.P., L.Z., Z.W. and X.L. analyzed the data and wrote the paper. All authors have read and agreed to the published version of the manuscript.

Funding: This research was supported by the National Natural Science Foundation of China (No: U23A20669) and the Sichuan Province Science and Technology Project “Research on Hydraulic turbine guide vane sediment wear characteristics and anti-wear coating materials” (No: JX-KY-2023-03).

Institutional Review Board Statement: This article does not contain any studies with human participants or animals performed by any of the authors.

Informed Consent Statement: Informed consent was obtained from all the individual participants included in this study.

Data Availability Statement: The raw data supporting the conclusions of this article will be made available by the authors on request.

Acknowledgments: This research was supported by Sichuan Provincial Engineering Research Center of Hydroelectric Energy Power Equipment Technology and Key Laboratory of Fluid Machinery and Engineering (Xihua University), Sichuan province.

Conflicts of Interest: Author Xiao Chang, Wenping Xiang was employed by the company Power China Hydropower Development Group Co., Ltd. and Gongzui Hydropower General Plant Dadu River Co., Ltd. The remaining authors declare that the research was conducted in the absence of any commercial or financial relationships that could be construed as a potential conflict of interest.

References

- Matsuo, Y.; Yanagisawa, A.; Yamashita, Y. A global energy outlook to 2035 with strategic considerations for Asia and Middle East energy supply and demand interdependencies. *Energy Strategy Rev.* **2013**, *2*, 79–91. [\[CrossRef\]](#)
- Neopane, H.P. *Sediment Erosion in Hydro Turbines*; Norwegian University of Science and Technology: Trondheim, Norway, 2010.
- Shen, Z.; Chu, W.; Dong, W. Effect of particle parameters on flow field and erosion wear characteristics of flow passage components in screw centrifugal pump. *Trans. Chin. Soc. Agric. Eng.* **2018**, *34*, 58–66.
- Shen, Z.J.; Chu, W.L.; Li, X.J.; Dong, W. Sediment Erosion in the Impeller of a Double-suction Centrifugal Pump-A case study of the Jingtai Yellow River Irrigation Project, China. *Wear* **2019**, *422*, 269–279. [\[CrossRef\]](#)
- Finnie, I. Some reflections on the past and future of erosion. *Wear* **1995**, *186*, 1–10. [\[CrossRef\]](#)
- Bitter, J.G.A. A study of erosion phenomena part I. *Wear* **1963**, *6*, 5–21. [\[CrossRef\]](#)
- Tilly, G.P.; Sage, W. The interaction of particle and material behaviour in erosion processes. *Wear* **1970**, *16*, 447–465. [\[CrossRef\]](#)
- Sheldon, G.L.; Kanhere, A. An investigation of impingement erosion using single particles. *Wear* **1972**, *21*, 195–209. [\[CrossRef\]](#)
- Hutchings, I.M. A model for the erosion of metals by spherical particles at normal incidence. *Wear* **1981**, *70*, 269–281. [\[CrossRef\]](#)
- Levy, A.; Mman, Y.F. Surface degradation of ductile metals in elevated temperature gas-particle streams. *Wear* **1986**, *111*, 173–186. [\[CrossRef\]](#)
- ANSYS. *ANSYS CFX-Solver: The Theory Guide*; ANSYS, Inc.: Canonsburg, PA, USA, 2019.
- Teran, L.A.; Aponte, R.D.; Munoz-Cubillos, J.; Roa, C.V.; Coronado, J.; Ladino, A.; Larrahondo, F.J.; Rodríguez, S.A. Analysis of economic impact from erosive wear by hard particles in a run-of-the-river hydroelectric plant. *Energy* **2016**, *113*, 1188–1201. [\[CrossRef\]](#)
- Gautam, S.; Neopane, H.P.; Acharya, N.; Chitrakar, S.; Thapa, B.S.; Zhu, B. Sediment erosion in low specific speed Francis turbines: A case study on effects and causes. *Wear* **2020**, *442/443*, 203152. [\[CrossRef\]](#)
- Thapa, B.S.; Dahlhaug, O.G.; Thapa, B. Sediment erosion in hydro turbines and its effect on the flow around guide vanes of francis turbine. *Renew. Sustain. Energy Rev.* **2015**, *49*, 1100–1113. [\[CrossRef\]](#)
- Lu, L.; Liu, J.; Yi, Y.; Liu, G. Evaluation on sand abrasion to Baihetan hydraulic turbines. *J. Hydroelectr. Eng.* **2016**, *35*, 67–74.
- Liu, G.; Li, Z. Analysis on the Abrasion of hydro-turbines due to sediment in the Lower Jinshajiang River. *Hydropower New Energy* **2017**, *4*, 2–5.
- Pang, J.; Liu, H.; Liu, X.; Yang, H.; Peng, Y.; Zeng, Y.; Yu, Z. Study on sediment erosion of high head Francis turbine runner in Minjiang River basin. *Renew. Energy* **2022**, *192*, 849–858. [\[CrossRef\]](#)
- Koirala, R.; Thapa, B.; Neopane, H.P.; Zhu, B. A review on flow and sediment erosion in guide vanes of Francis turbines. *Renew. Sustain. Energy Rev.* **2016**, *75*, 1054–1065. [\[CrossRef\]](#)
- Qian, Z.; Wang, Z.; Zhang, K.; Wu, Y.; Wu, Y. Analysis of silt abrasion and blade shape optimization in a centrifugal pump. *Proc. Inst. Mech. Eng. Part A J. Power Energy* **2014**, *228*, 585–591. [\[CrossRef\]](#)
- Saini, P.M. Study of silt erosion mechanism in Pelton turbine buckets. *Energy* **2012**, *39*, 286–293.
- Morales B, A.M.; Pachón, I.F.; Loboguerrero U, J.; Medina, J.A.; Escobar G, J.A. Development of a test rig to evaluate abrasive wear on Pelton turbine nozzles. A case study of Chivor Hydropower. *Wear* **2017**, *372–373*, 208–215. [\[CrossRef\]](#)
- Rai, A.K.; Kumar, A.; Staubli, T. Effect of concentration and size of sediments on hydro-abrasive erosion of Pelton turbine. *Renew. Energy* **2020**, *145*, 893–902. [\[CrossRef\]](#)
- Rai, A.K.; Kumar, A.; Staubli, T. Analytical modelling and mechanism of hydro-abrasive erosion in pelton buckets. *Wear* **2019**, *436–437*, 203003. [\[CrossRef\]](#)
- Rajkarnikar, B.; Neopane, H.P.; Thapa, B.S. Development of rotating disc apparatus for test of sediment-induced erosion in Francis runner blades. *Wear* **2013**, *306*, 119–125. [\[CrossRef\]](#)
- Krause, M.; Grein, H. Abrasion research and prevention. *Int. J. Hydropower Dams* **1996**, *3*, 17–20.
- Poudel, L.; Thapa, B.; Shrestha, B.P.; Thapa, B.S.; Shrestha, K.P.; Shrestha, N.K. Computational and experimental study of effects of sediment shape on erosion of hydraulic turbines. *Earth Environ. Sci.* **2012**, *15*, 032054. [\[CrossRef\]](#)
- Padhy, M.K.; Saini, R.P. A review on silt erosion in hydro turbines. *Renew. Sustain. Energy Rev.* **2008**, *12*, 1974–1987. [\[CrossRef\]](#)

28. Sugiyama, K.; Nakahama, S.; Hattori, S.; Nakano, K. Slurry wear and cavitation erosion of thermal sprayed cermets. *Wear* **2005**, *258*, 768–775. [[CrossRef](#)]
29. Liu, J.; Pang, J.; Liu, X.; Huang, Y.; Deng, H. Analysis of Sediment and Water Flow and Erosion Characteristics of Large Pelton Turbine Injector. *Processes* **2023**, *11*, 1011. [[CrossRef](#)]
30. Huang, Y.; Deng, F.; Deng, H.; Qing, Q.; Qin, M.; Liu, J.; Yu, Z.; Pang, J.; Liu, X. Study on Internal Flow Characteristics and Abrasive Wear of Pelton Turbine in Sand Laden Water. *Processes* **2023**, *11*, 1570. [[CrossRef](#)]
31. Deng, H.; Song, K.; Deng, F.; Huang, Y.; Luo, T.; Zhou, Y.; Qin, B.; Zeng, Y.; Yu, Z.; Pang, J.; et al. Nozzle Jet Deviation from Bucket Pitch Circle's Effect on the Stability and Efficiency of Pelton Turbine. *Processes* **2023**, *11*, 1342. [[CrossRef](#)]
32. Koirala, R.; Zhu, B.S.; Neopane, H.P. Effect of Guide Vane Clearance Gap on Francis Turbine Performance. *Energies* **2016**, *9*, 275. [[CrossRef](#)]
33. Noon, A.A.; Kim, M.H. Erosion wear on Francis turbine components due to sediment flow. *Wear* **2017**, *378*, 126–135. [[CrossRef](#)]
34. Koirala, R.; Thapa, B.; Neopane, H.P.; Zhu, B.; Chhetry, B. Sediment erosion in guide vanes of Francis turbine: A case study of Kaligandaki Hydropower Plant, Nepal. *Wear* **2016**, *362*, 53–60. [[CrossRef](#)]
35. Messa, G.V.; Mandelli, S.; Malavasi, S. Hydro-abrasive erosion in Pelton turbine injectors: A numerical study. *Renew. Energy* **2019**, *130*, 474–488. [[CrossRef](#)]
36. Leguizamon, S.; Jahanbakhsh, E.; Alimirzazadeh, S.; Maertens, A.; Avellan, F. Multiscale simulation of the hydroabrasive erosion of a Pelton bucket: Bridging scales to improve the accuracy. *Int. J. Turbomach. Propuls. Power* **2019**, *4*, 9. [[CrossRef](#)]
37. Chen, X.; Mclaury, B.S.; Shirazi, S.A. Application and experimental validation of a computational fluid dynamics (CFD)-based erosion prediction model in elbows and plugged tees. *Comput. Fluids* **2004**, *33*, 1251–1272. [[CrossRef](#)]
38. Mansouri, A.; Arabnejad, H.; Shirazi, S.A.; McLaury, B.S. A combined CFD/experimental methodology for erosion prediction. *Wear* **2015**, *332*, 1090–1097. [[CrossRef](#)]
39. Messa, G.V.; Malavasi, S. A CFD-based method for slurry erosion prediction. *Wear* **2018**, *398*, 127–145. [[CrossRef](#)]
40. Bahrainian, S.S.; Bakhshesh, M.; Hajidavalloo, E.; Parsi, M. A novel approach for solid particle erosion prediction based on Gaussian Process Regression. *Wear* **2020**, *466–467*, 203549. [[CrossRef](#)]
41. Dong, Y.; Si, F.; Cao, Y.; Jin, W.; Ren, S. A new mechanistic model for abrasive erosion using discrete element method. *Powder Technol.* **2020**, *11*, 380. [[CrossRef](#)]
42. Pang, J.; Liu, H.; Liu, X.; Ren, M.; Zhang, P.; Yu, Z. Analysis on the escape phenomenon of oil mist from turbine lower guide bearing based on VOF model. *Adv. Mech. Eng.* **2021**, *13*. [[CrossRef](#)]
43. Li, L.; Yan, D.; Liu, X.; Zhao, W.; Wang, Y.; Pang, J.; Wang, Z. Numerical Study on the Effect of Crown Clearance Thickness on High-Head Pump Turbines. *Water* **2023**, *15*, 3397. [[CrossRef](#)]

Disclaimer/Publisher's Note: The statements, opinions and data contained in all publications are solely those of the individual author(s) and contributor(s) and not of MDPI and/or the editor(s). MDPI and/or the editor(s) disclaim responsibility for any injury to people or property resulting from any ideas, methods, instructions or products referred to in the content.